Time-Delay Collaborative Control of Multiple Aerial Manipulators Using Nonsingular Terminal Sliding Mode

WU Zhiyu[1], *WANG Yaoyao*[1,2*], *WANG Hanzhuo*[1], *CHEN Jiawang*[3], *SUN Lizhuang*[4]

1. College of Mechanical and Electrical Engineering, Nanjing University of Aeronautics and Astronautics, Nanjing 210016, P. R. China; 2. State Key Laboratory of Mechanics and Control for Aerospace Structures, Nanjing 210016, P. R. China; 3. Donghai Laboratory, Zhoushan 316021, P. R. China; 4. China Academy of Machinery Beijing Research Institute of Mechanical & Electrical Technology Co., Ltd., Beijing 100044, P. R. China

(Received 29 May 2025; revised 8 August 2025; accepted 17 September 2025)

Abstract: To enhance the overall performance of multiple aerial manipulators under complex lumped disturbances, a nonsingular terminal sliding mode (NTSM) controller based on time-delay estimation (TDE) and deviation coupling control (DCC) is proposed. The stability of the controller is proven using the Lyapunov stability theory. Comparative experiments are conducted using a system of multiple aerial manipulators. The results demonstrate that, compared with a PID controller based on TDE, the proposed controller reduces the integral of absolute error (IAE), integral of time-weighted absolute error (ITAE), and integral of squared error (ISE) by at least 45.8%, 44.1%, and 66.5% respectively, thereby achieving superior overall control performance.

Key words: multiple aerial manipulators; time-delay estimation (TDE); terminal sliding mode; collaborative control

CLC number: TN925 **Document code:** A **Article ID:** 1005-1120(2026)02-0225-13

0 Introduction

An aerial manipulator, a robotic system comprising an unmanned aerial vehicle (UAV) platform and a robotic arm, integrates the UAV's agile maneuverability with the arm's operational capabilities[1]. Research in this domain has advanced significantly over the past decade, leading to the rapid diversification of its applications into fields such as the environment, trade, and the film industry[2-6]. However, conventional aerial manipulators typically employ rigid robotic arms whose considerable mass and high moment of inertia induce substantial disturbances on the UAV platform[7-8]. Moreover, the inherent limitations of individual systems in operational range and payload capacity restrict their efficacy for large-scale or highly complex tasks.

To mitigate disturbances from conventional rigid arms on the UAV platform and to further enhance overall system stability and flight endurance, lightweight and flexible designs become crucial development trends for the manipulator component of aerial robotic systems. Cable-driven technology, due to its flexible transmission mechanism, demonstrates significant potential. Cable-driven manipulators transmit actuation forces via flexible cables, enabling them to maintain operational capabilities while significantly reducing the dynamic disturbances exerted by the manipulator on the UAV platform[9]. Furthermore, in response to the escalating requirements for enhanced system workspace and redundancy when tackling highly complex tasks, multiple aerial manipulators have emerged as a more flexible and efficient solution. Through inter-agent communication and collaborative operation, multiple aerial manipulators can achieve spatial decomposition and parallel

*Corresponding author, E-mail address: yywang_cmee@nuaa.edu.cn.

How to cite this article: WU Zhiyu, WANG Yaoyao, WANG Hanzhuo, et al. Time-delay collaborative control of multiple aerial manipulators using nonsingular terminal sliding mode[J]. Transactions of Nanjing University of Aeronautics and Astronautics, 2026, 43(2): 225-237.

http://dx.doi.org/10.16356/j.1005-1120.2026.02.005

execution of tasks, thereby significantly enhancing the overall system's operational capability and reliability.

Specifically, although cable-driven systems offer the advantage of lower inertia, they introduce issues like elastic deformation and vibration, and the cable tension needs to be kept stable constinuously. These factors collectively result in a comparatively low control bandwidth for the system. Compounding this issue, the incorporation of cable-driven technology leads to a system of multiple aerial manipulators exhibiting intricate dynamics, which poses difficulties for accurate modeling. In addition, during coordinated tasks involving multiple aerial manipulators, inter-system dynamic coupling also presents additional challenges to control design and implementation. Conventional control methods often treat individual subsystems as decoupled[2] or rely on precise system models. Yet, when faced with the strong nonlinearities, parameter uncertainties, and complex inter-unit coupling inherent in cable-driven systems, these approaches find it challenging to guarantee desired control performance and robustness.

Time-delay control (TDC) is a model-free control strategy that is extensively recognized as a potent solution to the problems described above[10-11]. Usually, TDC contains two parts, named time-delay estimation (TDE) and injected dynamics. The former is used to achieve system dynamics and the latter is used to obtain desired performance, thereby significantly reducing the impact of modeling inaccuracies. Benefiting from this apparent advantage, TDC has found widespread application in various domains, including robotic manipulators[12-15], UAV positioning[16], space robots[17-18], etc. However, the utilization of TDE results in estimation error, i.e. TDE error. In order to mitigate the aforementioned error and improve the control precision of the system, the injected dynamics part is usually structured by robust control strategy, such as sliding mode control (SMC) and its variants[19-20], adaptive control[21-24], etc. SMC can achieve finite-time convergence of system states and strong robustness[25] by constructing a sliding surface. However, it still suffers from the chattering phenomenon, which adversely affects control smoothness in practical applications. To alleviate this problem, researchers have proposed higher-order sliding mode control (HOSMC) and terminal sliding mode control (TSMC). Chawengkrittayanont et al.[26] proposed a smooth second-order sliding mode controller for a class of multi-input multi-output mechanical systems with uncertain parameters and external disturbances. Xiong et al.[27] proposed a global fast dynamic TSMC method for performing the finite-time position and attitude tracking control of a small quadrotor UAV. By virtue of the design of a nonlinear sliding surface, rapid finite-time convergence of the system is achieved. However, in practical applications, TSMC suffers from a singularity problem, which may lead to the divergence of the control law. To overcome the singularity problem inherent in TSMC, Yao et al.[28] designed a nonsingular terminal sliding mode (NTSM) controller for the trajectory tracking control of free-flying space manipulators subject to uncertainties and disturbances. NTSM control[29-31] formulates a singularity-free nonlinear sliding surface by incorporating a combination of the tracking error and its derivative into its design. This design ensures the global boundedness and stability of the control law, while simultaneously preserving rapid and stable convergence properties and preventing the risk of control failure due to singularities.

Although there exist many works on sliding mode control for manipulator, in contrast to common ground-based, fixed-base manipulator or single-robot systems[32], the multiply aerial manipulators studied in this paper is characterized by strong coupling, underactuation, and multi-agent collaboration. This is particularly true for cable-driven systems with complex dynamics, where effectively integrating these techniques and introducing specialized coordination mechanisms to counteract inter-unit coupling disturbances remains a key challenge.

To further enhance the collaborative control performance of a system of multiple aerial manipulators, this paper proposes a system composed of multiple cable-driven aerial manipulators. For this pro-

posed system, an NTSM controller based on TDE and deviation coupling control (DCC) is designed to further optimize the overall system's coordination and control precision. The stability of the proposed controller is proven using the Lyapunov theory. Finally, the comprehensive performance of the proposed controller is validated through three sets of designed experiments.

The primary contributions we seek to make are as follows.

(1) Propose a novel NTSM controller combining TDE technique and DCC.

(2) Provide the stability analysis considering TDE and DCC.

(3) Verify the superiorities of our NTSM over the PID through comparative experiments.

1 Structural Design

The system of multiple aerial manipulators is composed of two aerial manipulator units. Each unit consists of a quadrotor UAV equipped with a robotic arm. These robotic arms utilize cable-driven technology, each featuring three active joints. The driving motors are proximally mounted, transmitting torque to the joints via drive cables. This configuration is designed to reduce the inertial torques generated during arm movement, thereby minimizing the manipulator's dynamic impact on the UAV platform.

The designed aerial manipulator is shown in Fig.1. The quadrotor has a wheelbase of 600 mm, is equipped with 15-inch propellers, and features an X-type configuration. The cable-driven robotic arm consists of two links and an end-effector, with a total length of 420 mm. The driving motors for the cable-driven robotic arm are mounted on the base of the quadrotor, with actuation forces transmitted to the joints through thin steel cables and pulley systems. Compared with conventional robotic arms, this configuration eliminates motors at the joints, leading to reduced disturbances on the UAV platform and lower power requirements. The detailed technical specifications are shown in Table 1.

Fig.1 Structure of aerial manipulator

Table 1 Technical specifications of aerial manipulars

Technical specification	Aerial manipulator 1	Aerial manipulator 2
Mass/ kg	3.75	3.67
Wheelbase/mm	600	600
Drive motor (UAV/manipulator)	Amov4006/Vishan EC1630	YH X4120/Vishan EC1630
Propeller size/mm	381	381
Flight controller	Codev dynamics (PX4)	Pixhawk 6c (PX4)
Onboard computer	Jetson Xavier NX	Jetson Xavier NX
Total length of manipulator/mm	420	420

2 Dynamic Modeling

To describe the mathematical model of the aerial manipulator, coordinate systems are established as shown in Fig.2. The coordinate frame system for the aerial manipulator comprises four main frames: An inertial frame $\{\boldsymbol{O}_{\mathrm{e}}\}$, an aerial manipulator's body frame $\{\boldsymbol{O}_{\mathrm{b}}\}$, manipulator joint frames $\{\boldsymbol{O}_{\mathrm{s}}\}$, and an end-effector frame $\{\boldsymbol{O}_{\mathrm{t}}\}$. The rotation matrix $\boldsymbol{R}_{\mathrm{b}}^{\mathrm{e}}$ from the body frame to the inertial frame is

$$\boldsymbol{R}_{\mathrm{b}}^{\mathrm{e}}=\begin{bmatrix}\cos\theta\cos\psi & \sin\phi\sin\theta\cos\psi-\cos\phi\sin\psi & \cos\phi\sin\theta\cos\psi+\sin\phi\sin\psi\\ \cos\theta\sin\psi & \sin\phi\sin\theta\sin\psi+\cos\phi\cos\psi & \cos\phi\sin\theta\sin\psi-\sin\phi\cos\psi\\ -\sin\theta & \sin\phi\cos\theta & \cos\phi\cos\theta\end{bmatrix} \tag{1}$$

The attitude of the aerial manipulator can be represented as $\boldsymbol{\Phi}=[\phi,\theta,\psi]^{\mathrm{T}}$, where ϕ, θ and ψ are the roll, the pitch, and the yaw angles of the aerial manipulator, respectively.

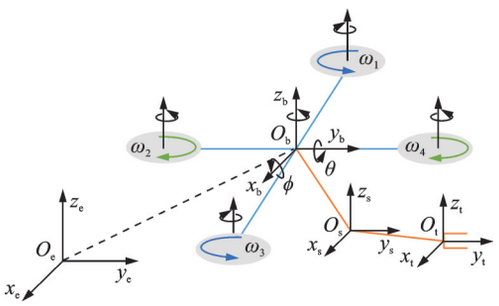

Fig.2 Reference frames for an aerial manipulator

Adopting an independent modeling approach, the dynamic model of the aerial manipulator is derived based on fundamental principles of dynamics and the Newton-Euler formulation as[33]

$$\begin{cases} m\ddot{\boldsymbol{p}}-mg\boldsymbol{e}_3=\boldsymbol{f}+\boldsymbol{f}_{\mathrm{d}} \\ \boldsymbol{f}=f_{\mathrm{b}}\boldsymbol{R}_{\mathrm{b}}^{\mathrm{e}}\boldsymbol{e}_3 \\ \boldsymbol{J}\dot{\boldsymbol{\omega}}+\boldsymbol{\omega}\times\boldsymbol{J}\boldsymbol{\omega}=\boldsymbol{\tau}+\boldsymbol{\tau}_{\mathrm{d}} \end{cases} \tag{2}$$

where m is the mass of the aerial manipulator; $\boldsymbol{f}$ the total thrust vector acting on the aerial manipulator and expressed in the inertial frame; $\boldsymbol{J}$ the inertia matrix of the aerial manipulator; $\boldsymbol{p}$ the position of the aerial manipulator; $\boldsymbol{\omega}$ the angular velocity of the aerial manipulator; $\boldsymbol{e}_3$ a unit vector in the inertial frame; f_{b} the total thrust generated by the propellers, acting on the aerial manipulator and expressed in the body frame; $\boldsymbol{f}_{\mathrm{d}}$ the vector of coupling forces between the UAV platform and the robotic arm, combined with other complex external force disturbances; $\boldsymbol{\tau}$ the total control torque acting on the aerial manipulator $\boldsymbol{\tau}=[\tau_x,\tau_y,\tau_z]^{\mathrm{T}}$; and $\boldsymbol{\tau}_{\mathrm{d}}$ the vector of coupling torques between the UAV platform and the robotic arm, combined with other complex external torque disturbances.

In the aerial manipulator designed in this paper, the UAV platform is an X-configuration quadrotor. f_{b} and $\boldsymbol{\tau}$ are given as

$$\begin{bmatrix} f_{\mathrm{b}} \\ \tau_x \\ \tau_y \\ \tau_z \end{bmatrix}= \begin{bmatrix} c_{\mathrm{T}} & c_{\mathrm{T}} & c_{\mathrm{T}} & c_{\mathrm{T}} \\ -\frac{\sqrt{2}}{2}dc_{\mathrm{T}} & \frac{\sqrt{2}}{2}dc_{\mathrm{T}} & \frac{\sqrt{2}}{2}dc_{\mathrm{T}} & -\frac{\sqrt{2}}{2}dc_{\mathrm{T}} \\ \frac{\sqrt{2}}{2}dc_{\mathrm{T}} & -\frac{\sqrt{2}}{2}dc_{\mathrm{T}} & \frac{\sqrt{2}}{2}dc_{\mathrm{T}} & -\frac{\sqrt{2}}{2}dc_{\mathrm{T}} \\ c_{\mathrm{M}} & c_{\mathrm{M}} & -c_{\mathrm{M}} & -c_{\mathrm{M}} \end{bmatrix} \begin{bmatrix} \tilde{\omega}_1^2 \\ \tilde{\omega}_2^2 \\ \tilde{\omega}_3^2 \\ \tilde{\omega}_4^2 \end{bmatrix} \tag{3}$$

where c_{T} is the propeller thrust coefficient; c_{M} the propeller torque coefficient; d the distance from the center of the aerial manipulator's body to each propeller; and $\tilde{\omega}_i\,(i=1,2,3,4)$ the rotational speeds of the four propellers.

The aerial manipulator exhibits time-varying dynamic parameters whose influence is non-negligible. The variations in these dynamic parameters are as follows

$$\begin{cases} m=m_0+\Delta m \\ \boldsymbol{J}=\boldsymbol{J}_0+\Delta\boldsymbol{J} \end{cases} \tag{4}$$

where m_0 and $\boldsymbol{J}_0$ are the nominal dynamic parameters; and Δm and $\Delta\boldsymbol{J}$ the variations in dynamic parameters caused by the robotic arm's operation and external disturbances. By lumping together the unknown terms and other disturbances, and by introducing constant diagonal matrices $\bar{\boldsymbol{m}}$ and $\bar{\boldsymbol{J}}$, Eq.(2) can be rewritten as

$$\begin{cases} \bar{\boldsymbol{m}}\ddot{\boldsymbol{p}}+\boldsymbol{\xi}=\boldsymbol{f} \\ \bar{\boldsymbol{J}}\dot{\boldsymbol{\omega}}+\boldsymbol{\mu}=\boldsymbol{\tau} \end{cases} \tag{5}$$

$$\begin{cases} \boldsymbol{\xi}=(m-\bar{\boldsymbol{m}})\ddot{\boldsymbol{p}}-mg\boldsymbol{e}_3-\boldsymbol{f}_{\mathrm{d}} \\ \boldsymbol{\mu}=(\boldsymbol{J}-\bar{\boldsymbol{J}})\dot{\boldsymbol{\omega}}+\boldsymbol{\omega}\times\boldsymbol{J}\dot{\boldsymbol{\omega}}-\boldsymbol{\tau}_{\mathrm{d}} \end{cases} \tag{6}$$

The terms $\boldsymbol{\xi}$ and $\boldsymbol{\mu}$ encompass variations in the dynamic parameters of the aerial manipulator system as well as external disturbances. Due to their complex form and the difficulty in obtaining their precise values, the TDE technique is employed to determine their approximate values, shown as

$$\begin{cases} \hat{\boldsymbol{\xi}}=\boldsymbol{\xi}_{(t-L)}=\boldsymbol{f}_{(t-L)}-\bar{\boldsymbol{m}}\ddot{\boldsymbol{p}}_{(t-L)} \\ \hat{\boldsymbol{\mu}}=\boldsymbol{\mu}_{(t-L)}=\boldsymbol{\tau}_{(t-L)}-\bar{\boldsymbol{J}}\ddot{\boldsymbol{\Phi}}_{(t-L)} \end{cases} \tag{7}$$

where L stands for delayed time and is often selected as one or some sampling periods.

3 Design of NTSM Controller

For a single aerial manipulator, the quadrotor serves as the primary mobile platform, responsible

for large-scale positional movements. The robotic arm is mainly tasked with controlling the end-effector's attitude and making fine adjustments to its position over a smaller range. This paper primarily focuses on the control of the quadrotor. The controller is designed using a dual closed-loop architecture, with an outer loop for position control and an inner loop for attitude control. Given that a system of multiple aerial manipulators is highly dependent on positional accuracy, a DCC strategy is designed and incorporated into the position controller. This strategy aims to establish dynamic collaborative relationships among the individual aerial manipulator units, thereby enhancing overall control consistency and robustness. The designed controller structure is shown in Fig.3.

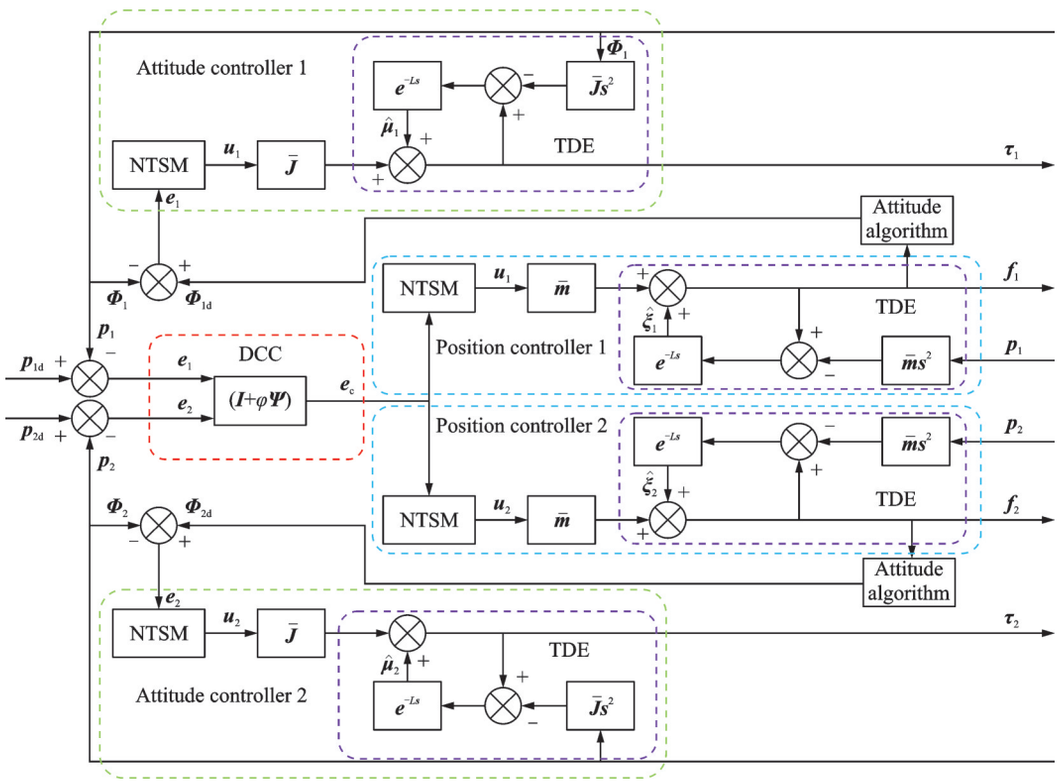

Fig.3 Control structure for multiple aerial manipulators

3.1 Position controller design

To enhance the collaborative control performance of the system, this paper designs a position controller based on DCC. Initially, the synchronization error and coupled error variable are designed as

$$\boldsymbol{e}_{\mathrm{s}}=\boldsymbol{\Psi}\boldsymbol{e} \tag{8}$$

$$\boldsymbol{e}_{\mathrm{c}}=\boldsymbol{e}+\varphi\boldsymbol{e}_{\mathrm{s}}=(\mathrm{I}+\varphi\boldsymbol{\Psi})\boldsymbol{e} \tag{9}$$

where $\boldsymbol{e}=\boldsymbol{p}_{\mathrm{d}}-\boldsymbol{p}$ is the tracking error vector for aerial manipulators and $\boldsymbol{p}_{\mathrm{d}}$ the desired trajectory; $\boldsymbol{e}_{\mathrm{s}}$ and $\boldsymbol{e}_{\mathrm{c}}$ stand for the vectors of synchronization error and deviation coupling error; φ is the relative-coupling coefficient diagonal positive matrix; and $\boldsymbol{\Psi}$ the synchronization coefficient matrix and designed as

$$\boldsymbol{\Psi}=\boldsymbol{I}-\frac{1}{n}\boldsymbol{\Theta} \tag{10}$$

where $\boldsymbol{I}$ stands for the unit matrix and $\boldsymbol{\Theta}$ the matrix with all entries as 1.

Combining Eq.(8) and Eq.(10), we obtain

$$e_{si}=e_i-\frac{\sum_{j=1}^{n}e_j}{n}=\frac{(e_i-e_1)+\cdots+(e_i-e_n)}{n} \tag{11}$$

The design of SMC typically involves two phases. The first is the reaching phase, in which a control law is designed to ensure the system states reach a predefined sliding surface in finite time. The second is the sliding phase, where once on the surface, the system states slide along it and ultimately converge to the equilibrium point[34]. However, SMC suffers from a high-frequency switching action known as chattering. This phenomenon, caused by the sign function or discontinuous switching terms,

can excite unmodeled high-frequency dynamics in the system, leading to actuator wear and even instability[35]. Employing the reaching law method can improve the dynamic quality of the reaching motion and mitigate chattering.

Define the sliding mode surface function as

$$\boldsymbol{s}=\boldsymbol{e}_{\mathrm{c}}+\boldsymbol{\alpha}\mathrm{sig}(\dot{\boldsymbol{e}}_{\mathrm{c}})^{\beta} \tag{12}$$

The reaching law is chosen as

$$\dot{\boldsymbol{s}}=-|\dot{\boldsymbol{e}}_{\mathrm{c}}|^{\beta-1}\left(\boldsymbol{\sigma}_1\boldsymbol{s}+\boldsymbol{\sigma}_2\mathrm{sig}(\boldsymbol{s})^{\gamma}\right) \tag{13}$$

where $\boldsymbol{s}\in\mathbf{R}^3$, $\boldsymbol{\alpha}=\mathrm{diag}([\alpha_1,\alpha_2,\alpha_3])$, $1<\beta_i<2$. $\mathrm{sig}(\dot{e}_{ci})^{\beta_i}=|\dot{e}_{ci}|^{\beta_i}\mathrm{sign}(\dot{e}_{ci})$, $\mathrm{d}\left(\mathrm{sig}(\dot{e}_{ci})^{\beta_i}\right)/\mathrm{d}t=\beta_i|\dot{e}_{ci}|^{\beta_i-1}\ddot{e}_{ci}$. $\boldsymbol{\sigma}_1=\mathrm{diag}(\sigma_{11},\sigma_{12},\sigma_{13})$, $\sigma_{1i}>0$; $\boldsymbol{\sigma}_2=\mathrm{diag}(\sigma_{21},\sigma_{22},\sigma_{23})$, $\sigma_{2i}>0$; $\boldsymbol{\gamma}=\mathrm{diag}(\gamma_1,\gamma_2,\gamma_3)$, $0<\gamma_i<1$.

In Eq.(13), Term $-|\dot{\boldsymbol{e}}_{\mathrm{c}}|^{\beta-1}\boldsymbol{\sigma}_1\boldsymbol{s}$ ensures that when the sliding mode surface $\boldsymbol{s}$ is large, the system states approach the sliding mode at a high speed, with the convergence rate determined by $\boldsymbol{\sigma}_1$; term $-|\dot{\boldsymbol{e}}_{\mathrm{c}}|^{\beta-1}\boldsymbol{\sigma}_2\mathrm{sig}(\boldsymbol{s})^{\gamma}$, through the adjustment of $\boldsymbol{\sigma}_2$, guarantees a high reaching speed when $\boldsymbol{s}$ is large, while ensuring a small control gain when $\boldsymbol{s}$ is small to reduce chattering. Furthermore, both the sliding surface and the reaching law selected in this paper are continuous functions without any discontinuous terms, which also serves to mitigate chattering.

Theorem 1 Let us consider NTSM $\boldsymbol{s}$ in Eq.(12), the coupled error $\boldsymbol{e}_{\mathrm{c}}$ and tracking error $\boldsymbol{e}$ in Eq.(9), there exists a short time interval T, when the sliding surface is bounded, i.e., $|\boldsymbol{s}|\leqslant\Delta$, the proposed NTSM can guarantee that the tracking error $\boldsymbol{e}$ converges to region $\Omega_e=\{\boldsymbol{e}||\boldsymbol{e}|\leqslant(\boldsymbol{I}+\boldsymbol{\varphi}\boldsymbol{\Psi})^{-1}\cdot 2\Delta\}$, where Δ can be significantly small. That is, the position $\boldsymbol{p}$ of the aerial manipulator would converge to its desired position signal $\boldsymbol{p}_{\mathrm{d}}$ within a bounded and significantly small tracking error. The boundedness of tracking error $\boldsymbol{e}$ by using the proposed NTSM is discussed later.

Combining Eqs.(5, 7, 12, 13), the NTSM controller could be obtained as

$$\boldsymbol{f}=\bar{\boldsymbol{m}}\Big(\ddot{\boldsymbol{p}}_{\mathrm{d}}+\boldsymbol{\alpha}^{-1}\boldsymbol{\beta}^{-1}(\boldsymbol{I}+\boldsymbol{\varphi}\boldsymbol{\Psi})^{-1}\Big(\mathrm{sig}(\dot{\boldsymbol{e}}_{\mathrm{c}})^{2-\beta}+\boldsymbol{\sigma}_1\boldsymbol{s}+\boldsymbol{\sigma}_2\mathrm{sig}(\boldsymbol{s})^{\gamma}\Big)\Big)+\boldsymbol{f}_{(t-L)}-\bar{\boldsymbol{m}}\ddot{\boldsymbol{p}}_{(t-L)} \tag{14}$$

The acceleration $\ddot{\boldsymbol{p}}_{(t-L)}$ can be obtained by performing a second-order difference on the position signal $\boldsymbol{p}$ as

$$\ddot{\boldsymbol{p}}_{(t-L)}=(\boldsymbol{p}-2\boldsymbol{p}_{(t-L)}+\boldsymbol{p}_{(t-2L)})/L^2 \tag{15}$$

Combining Eqs.(7, 4), the error dynamics of the control system is

$$(\boldsymbol{I}+\boldsymbol{\varphi}\boldsymbol{\Psi})\bar{\boldsymbol{m}}^{-1}\left(\boldsymbol{\xi}-\hat{\boldsymbol{\xi}}\right)=\ddot{\boldsymbol{e}}_{\mathrm{c}}+\boldsymbol{\alpha}^{-1}\boldsymbol{\beta}^{-1}\left(\mathrm{sig}(\dot{\boldsymbol{e}}_{\mathrm{c}})^{2-\beta}+\boldsymbol{\sigma}_1\boldsymbol{s}+\boldsymbol{\sigma}_2\mathrm{sig}(\boldsymbol{s})^{\gamma}\right) \tag{16}$$

where $(\boldsymbol{I}+\boldsymbol{\varphi}\boldsymbol{\Psi})\bar{\boldsymbol{m}}^{-1}\left(\boldsymbol{\xi}-\hat{\boldsymbol{\xi}}\right)$ represents the error generated by using TDE technology, represented by $\boldsymbol{\varepsilon}$, as follows

$$\boldsymbol{\varepsilon}=(\boldsymbol{I}+\boldsymbol{\varphi}\boldsymbol{\Psi})\bar{\boldsymbol{m}}^{-1}\left(\boldsymbol{\xi}-\hat{\boldsymbol{\xi}}\right) \tag{17}$$

The prerequisite for the error $\boldsymbol{\varepsilon}$ to be bounded is that the absolute value of each eigenvalue of the matrix $\boldsymbol{I}-(\boldsymbol{I}+\boldsymbol{\varphi}\boldsymbol{\Psi})\bar{\boldsymbol{m}}^{-1}\bar{\boldsymbol{m}}(\boldsymbol{I}+\boldsymbol{\varphi}\boldsymbol{\Psi})^{-1}$ is less than 1.

3.2 Attitude controller design

The selection of the sliding surface and reaching law for the attitude controller is identical to that for the position controller. Similarly, the output of the attitude controller can be obtained as

$$\boldsymbol{\tau}=\bar{\boldsymbol{J}}\Big(\ddot{\boldsymbol{\Phi}}_{\mathrm{d}}+\boldsymbol{\alpha}_{\Phi}^{-1}\boldsymbol{\beta}_{\Phi}^{-1}\Big(\mathrm{sig}(\dot{\boldsymbol{e}})^{2-\beta_{\Phi}}+\boldsymbol{\sigma}_{\Phi 1}\boldsymbol{s}+\boldsymbol{\sigma}_{\Phi 2}\mathrm{sig}(\boldsymbol{s})^{\gamma_{\Phi}}\Big)\Big)+\boldsymbol{\tau}_{(t-L)}-\bar{\boldsymbol{J}}\ddot{\boldsymbol{\Phi}}_{(t-L)} \tag{18}$$

where $\boldsymbol{\Phi}_{\mathrm{d}}$ is the desired attitude.

The desired attitude of the aerial manipulator is determined by the position loop. Substituting Eq.(14) into Eq.(2), we obtain

$$f_{\mathrm{b}}\boldsymbol{R}_{\mathrm{b}}^{\mathrm{e}}\boldsymbol{e}_3=f_{\mathrm{b}}\begin{bmatrix}\cos\phi_{\mathrm{d}}\sin\theta_{\mathrm{d}}\cos\psi_{\mathrm{d}}+\sin\phi_{\mathrm{d}}\sin\psi_{\mathrm{d}}\\ \cos\phi_{\mathrm{d}}\sin\theta_{\mathrm{d}}\sin\psi_{\mathrm{d}}-\sin\phi_{\mathrm{d}}\cos\psi_{\mathrm{d}}\\ \cos\phi_{\mathrm{d}}\cos\theta_{\mathrm{d}}\end{bmatrix}=\boldsymbol{f} \tag{19}$$

where $\boldsymbol{f}$ is the output of the position controller, $\boldsymbol{f}=[f_1,f_2,f_3]^{\mathrm{T}}$. Given a desired yaw angle ψ_{d}, all attitude angles are constrained within the following ranges

$$-\frac{\pi}{2}\leqslant\phi_{\mathrm{d}}\leqslant\frac{\pi}{2},-\frac{\pi}{2}\leqslant\theta_{\mathrm{d}}\leqslant\frac{\pi}{2},-\pi\leqslant\psi_{\mathrm{d}}\leqslant\pi \tag{20}$$

The desired attitude angles can then be calculated as

$$\begin{cases}\phi_{\mathrm{d}}=\arcsin\left(\sin\psi_{\mathrm{d}}\dfrac{f_1}{|f|}-\cos\psi_{\mathrm{d}}\dfrac{f_3}{|f|}\right)\\ \theta_{\mathrm{d}}=\arctan\left(\left(\cos\psi_{\mathrm{d}}\dfrac{f_1}{|f|}+\sin\psi_{\mathrm{d}}\dfrac{f_2}{|f|}\right)\Big/\dfrac{f_3}{|f|}\right)\end{cases}\tag{21}$$

3.3 Proof of stability

For convenience and without loss of generality, we select a single direction here to present the derivation and proof of stability for the controller. The following two lemmas are given before proving the stability of the controller.

Lemma 1 When $a_1, a_2, \cdots, a_n \in \mathbf{R}^+$, and $0<p<2$, the following inequality hold

$$(a_1^2+a_2^2+\cdots+a_n^2)^p \leqslant (a_1^p+a_2^p+\cdots+a_n^p)^2 \tag{22}$$

Lemma 2 Suppose a Lyapunov function $V(x)$ satisfies the inequality as

$$\dot{V}(x)+\alpha V(x)+\beta V^{\gamma}(x)\leqslant 0 \tag{23}$$

where $0<\gamma<1$, then the finite time T for $V(x)$ to converge from the initial value $V(x_0)$ to $V(0)$ satisfies

$$T\leqslant\frac{1}{\alpha(1-\gamma)}\ln\frac{\alpha V^{1-\gamma}(x_0)+\beta}{\beta} \tag{24}$$

Choose a Lyapunov function as

$$V=0.5s_i^2 \tag{25}$$

By differentiating Eq.(25) and substituting Eqs.(12, 16, 17) into it gives the following form

$$\dot{V}=s_i\dot{s}_i=-s_i|\dot{e}_{ci}|^{\beta_i-1}\left(\sigma_{1i}s_i+\sigma_{2i}\mathrm{sig}(s_i)^{\gamma_i}-\alpha_i\beta_i\varepsilon_i\right) \tag{26}$$

Eq.(26) can be transformed as

$$\dot{V}=-s_i|\dot{e}_{ci}|^{\beta_i-1}\left[\left(\sigma_{1i}-\frac{\alpha_i\beta_i\varepsilon_i}{s_i}\right)s_i+\sigma_{2i}\mathrm{sig}(s_i)^{\gamma_i}\right] \tag{27}$$

$$\dot{V}=-s_i|\dot{e}_{ci}|^{\beta_i-1}\left[\sigma_{1i}s_i+\mathrm{sig}(s_i)^{\gamma_i}\left(\sigma_{2i}-\frac{\alpha_i\beta_i\varepsilon_i}{\mathrm{sig}(s_i)^{\gamma_i}}\right)\right] \tag{28}$$

Let $K_1=(\sigma_{1i}-\alpha_i\beta_i\varepsilon_i/s_i)|\dot{e}_{ci}|^{\beta_i-1}$, $K_2=\sigma_{2i}|\dot{e}_{ci}|^{\beta_i-1}$, then Eq.(27) can be further transformed as

$$\dot{V}=-s_iK_1s_i-s_iK_2\mathrm{sig}(s_i)^{\gamma} \tag{29}$$

When $\dot{e}_{\mathrm{c}}\neq 0$, and $\bar{K}_1>0$, $\bar{K}_2>0$, the following inequality holds according to Lemma 1

$$\dot{V}\leqslant -2\bar{K}_1V-2^{\frac{\gamma_i+1}{2}}\bar{K}_2V^{\frac{\gamma_i+1}{2}} \tag{30}$$

where $\bar{K}_1=\min\{K_{1i}\}$, $\bar{K}_2=\min\{K_{2i}\}$.

According to Lemma 2, the time T_{s} required for reaching phase satisfies

$$T_{\mathrm{s}}\leqslant\frac{1}{2\bar{K}_1(1-\gamma_i)}\ln\left(\frac{2\bar{K}_1V^{(1-\gamma_i)/2}}{2^{(1-\gamma_i)/2}\bar{K}_2}+1\right) \tag{31}$$

The phase trajectory of the system will converge into the following spherical domain in a finite time since $\bar{K}_1>0$

$$|s_i|\leqslant\frac{\alpha_i\beta_i|\varepsilon_i|}{\sigma_{1i}} \tag{32}$$

By analyzing Eq.(28) similarly to Eq.(27), it can be obtained that the phase trajectory of the system will converge into the following spherical domain in a finite time as

$$|s_i|\leqslant\left(\frac{\alpha_i\beta_i|\varepsilon_i|}{\sigma_{2i}}\right)^{\frac{1}{\gamma_i}} \tag{33}$$

Thus, the phase trajectory of the system can converge into the following neighborhood as

$$|s_i|\leqslant\Delta=\min\{\Delta_1,\Delta_2\} \tag{34}$$

where $\Delta_1=\alpha_i\beta_i|\varepsilon_i|/\sigma_{1i}$, $\Delta_2=(\alpha_i\beta_i|\varepsilon_i|/\sigma_{2i})^{1/\gamma_i}$.

When $\dot{e}_{\mathrm{c}}=0$, $\dot{V}=0$, the second derivative of the coupling error can be obtained as

$$\ddot{e}_{ci}=-\frac{1}{\alpha_i\beta_i}\mathrm{sig}(\dot{e}_{ci})^{2-\beta_i}-\frac{1}{\alpha_i\beta_i}\left(\sigma_{1i}s_i+\sigma_{2i}\mathrm{sig}(s_i)^{\gamma_i}\right)+\varepsilon_i \tag{35}$$

Eq.(35) can be transformed into two forms as

$$\ddot{e}_{ci}=-\frac{1}{\alpha_i\beta_i}\left[\mathrm{sig}(\dot{e}_{ci})^{2-\beta_i}+\left(\sigma_{1i}-\frac{\alpha_i\beta_i\varepsilon_i}{s_i}\right)s_i+\sigma_{2i}\mathrm{sig}(s_i)^{\gamma_i}\right] \tag{36}$$

$$\ddot{e}_{ci}=-\frac{1}{\alpha_i\beta_i}\left[\mathrm{sig}(\dot{e}_{ci})^{2-\beta_i}+\sigma_{1i}s_i+\left(\sigma_{2i}-\frac{\alpha_i\beta_i\varepsilon_i}{\mathrm{sig}(s_i)^{\gamma_i}}\right)\mathrm{sig}(s_i)^{\gamma_i}\right] \tag{37}$$

When $s_i\notin\Delta$, it can be seen that $\ddot{e}_{ci}\neq 0$ from Eqs.(36, 37), which means that the system will not stay in the state of $\dot{e}_{\mathrm{c}}=0$ and $s_i\notin\Delta$, and can still reach the neighborhood Δ in a finite time.

Afterwards, taking a single direction to analyze, substituting Eq.(34) into Eq.(12), we have

$$s_i=e_{ci}+\alpha_i\mathrm{sig}(\dot{e}_{ci})^{\beta_i}\leqslant\Delta \tag{38}$$

Transform Eq.(38) to the following form as

$$e_{ci}+\left(\alpha_i-\frac{s_i}{\mathrm{sig}(\dot{e}_{ci})^{\beta_i}}\right)\mathrm{sig}(\dot{e}_{ci})^{\beta_i}=0 \tag{39}$$

When $\alpha_i-s_i/\mathrm{sig}(\dot{e}_{ci})^{\beta_i}>0$, Eq.(39) still remains the form of NTSM. Therefore, the coupling error will converge into the following spherical domain in a finite time

$$|\dot{e}_{ci}|\leqslant\left(\frac{|s_i|}{\alpha_i}\right)^{1/\beta_i}\leqslant\left(\frac{\Delta}{\alpha_i}\right)^{1/\beta_i} \tag{40}$$

According to Eqs.(39, 40), we have

$$e_{ci}=\left|s_i-\alpha_i\mathrm{sig}(\dot{e}_{ci})^{\beta_i}\right|\leqslant|s_i|+\left|-\alpha_i\mathrm{sig}(\dot{e}_{ci})^{\beta_i}\right|\leqslant 2\Delta \tag{41}$$

Finally, the boundedness of the control error $\boldsymbol{e}$ is proved. From Eq.(9), it can be obtained that

$$\boldsymbol{e}=(\boldsymbol{I}+\boldsymbol{\varphi}\boldsymbol{\Psi})^{-1}\boldsymbol{e}_{\mathrm{c}} \tag{42}$$

Combining Eqs.(41, 42), the control error will converge into the following spherical domain

$$|e_i|<|(\boldsymbol{I}+\boldsymbol{\varphi}\boldsymbol{\Psi})^{-1}\cdot 2\Delta| \tag{43}$$

Proof Completed.

4 Experiments

To validate the effectiveness of the proposed controller, comparative experiments are conducted on a multi-aerial manipulator experimental platform. Three sets of these comparative experiments are designed in this paper. Specifically, Experiment 1 is a performance comparison between a PID controller based on TDE and the proposed controller. Experiment 2 compares the performance of the proposed controller under two distinct operating conditions, with the robotic arm in motion and when it is stationary, to validate the robustness of the proposed controller. Experiment 3 evaluates the performance of the proposed controller with and without DCC, thereby verifying the effectiveness of the DCC itself.

The multi-aerial-manipulator experimental platform is made up of two aerial manipulator units. Each unit utilizes a PX4 flight controller and employs GPS for positioning. Furthermore, all units are equipped with a Jetson Xavier NX onboard computer running the robot operating system (ROS) for control in offboard mode.

Communication among the units is established over a common local area network (LAN) to enable collaborative control. The control algorithm is executed on the onboard computer with an execution period of 20 ms. The relative coupling coefficient $\boldsymbol{\varphi}$ is set to $\boldsymbol{I}$ and the delayed time L to 20 ms. Table 2 presents the selected controller parameters. The controller parameters listed in Table 2 are obtained via a two-stage process combining simulation and real-world experimentation. Initially, a baseline set of parameters is established through simulation, and then fine-tuned on the physical platform using a trial-and-error method guided by the actual tracking performance. In this control design, the parameters $\bar{\boldsymbol{m}}$ and $\bar{\boldsymbol{J}}$ govern the controller's overall gain, where larger values yield faster convergence at the risk of increased chattering. The parameter $\boldsymbol{\alpha}$ sets the weight of the error derivative term within the sliding

Table 2 Parameters of controller

Controller	Parameter	
	Aerial manipulator 1	Aerial manipulator 2
NTSM	$\bar{\boldsymbol{m}}=[0.16,0.16,0.36]$ $\bar{\boldsymbol{J}}=[0.05,0.05,0.02]$ $\boldsymbol{\alpha}=[2,2,2]$ $\boldsymbol{\alpha}_{\Phi}=[0.8,0.8,0.8]$ $\boldsymbol{\beta}=[1.2,1.2,1.2]$ $\boldsymbol{\beta}_{\Phi}=[1.6,1.6,1.6]$ $\boldsymbol{\gamma}=[0.6,0.6,0.6]$ $\boldsymbol{\gamma}_{\Phi}=[0.6,0.6,0.6]$ $\boldsymbol{\sigma}_1=[1.6,1.6,4]$ $\boldsymbol{\sigma}_{\Phi 1}=[10,10,10]$ $\boldsymbol{\sigma}_2=[6.4,6.4,8]$ $\boldsymbol{\sigma}_{\Phi 2}=[10,10,10]$	$\bar{\boldsymbol{m}}=[0.14,0.14,0.32]$ $\bar{\boldsymbol{J}}=[0.05,0.05,0.02]$ $\boldsymbol{\alpha}=[2,2,2]$ $\boldsymbol{\alpha}_{\Phi}=[0.8,0.8,0.8]$ $\boldsymbol{\beta}=[1.2,1.2,1.2]$ $\boldsymbol{\beta}_{\Phi}=[1.6,1.6,1.6]$ $\boldsymbol{\gamma}=[0.6,0.6,0.6]$ $\boldsymbol{\gamma}_{\Phi}=[0.6,0.6,0.6]$ $\boldsymbol{\sigma}_1=[1.5,1.5,4]$ $\boldsymbol{\sigma}_{\Phi 1}=[10,10,10]$ $\boldsymbol{\sigma}_2=[6,6,8]$ $\boldsymbol{\sigma}_{\Phi 2}=[10,10,10]$
PID	$\bar{\boldsymbol{m}}=[0.12,0.12,0.1]$ $\bar{\boldsymbol{J}}=[0.06,0.06,0.02]$ $\boldsymbol{k}_{\mathrm{P}}=[3,3,5]$ $\boldsymbol{k}_{\Phi\mathrm{P}}=[1,1,1]$ $\boldsymbol{k}_{\mathrm{I}}=[0.4,0.4,2]$ $\boldsymbol{k}_{\Phi\mathrm{I}}=[0.2,0.2,0.1]$ $\boldsymbol{k}_{\mathrm{D}}=[0.2,0.2,0]$ $\boldsymbol{k}_{\Phi\mathrm{D}}=[0.003,0.003,0]$	$\bar{\boldsymbol{m}}=[0.095,0.095,0.1]$ $\bar{\boldsymbol{J}}=[0.06,0.06,0.02]$ $\boldsymbol{k}_{\mathrm{P}}=[1.8,1.8,4]$ $\boldsymbol{k}_{\Phi\mathrm{P}}=[0.14,0.14,0.2]$ $\boldsymbol{k}_{\mathrm{I}}=[0.4,0.4,2]$ $\boldsymbol{k}_{\Phi\mathrm{I}}=[0.3,0.3,0.1]$ $\boldsymbol{k}_{\mathrm{D}}=[0.2,0.2,0]$ $\boldsymbol{k}_{\Phi\mathrm{D}}=[0.04,0.04,0]$

surface, thus shaping the dynamic response. The nonlinearity of the convergence is influenced by β, with values approaching 1 and accelerating convergence during the reaching phase. The reaching law parameters, σ_1 and σ_2, dictate the speed of approach to the sliding surface; higher values result in a faster reaching phase and cause more intense chattering. Finally, γ as an exponent in a nonlinear term, is used to speed up convergence near the sliding surface

The trajectory selected for the three sets of experiments is as follows: $x_d = 2\cos(0.4t) - 2$, $y_d = 2\sin(0.4t)$, $z_d = 2$, $\psi_d = 0$.

The results of Experiment 1 are shown in Fig.4, where Xe_1 and Ye_1 denote the tracking errors of the first aerial manipulator along the x- and y-axes, respectively, while Xe_2 and Ye_2 denote those of the second aerial manipulator. Based on these experimental results, the proposed NTSM controller demonstrates performance significantly superior to that of the PID controller based on TDE, characterized by faster convergence speed and smaller peak errors.

Table 3 presents the integral of absolute error (IAE), integral of time-weighted absolute error (ITAE), and integral of squared error (ISE) of the tracking performance for the various controllers in Experiment 1, along both the X and Y axes. The proposed NTSM controller demonstrates significant improvements over the benchmark PID-based controllers: Its IAE is reduced by 45.8%, 65.0%, 66.6% and 60.5%,. It indicates that the overall control precision of the proposed NTSM controller is significantly superior to that of the PID controller. Its ITAE is reduced by 44.1%, 64.8%, 66.5% and 59.5%. It indicates that the PID controller produces significant instantaneous errors or overshoot, whereas the proposed NTSM controller successfully suppresses these large-magnitude errors. Its ISE is reduced by 66.5%, 85.8%, 90.3%, and 86.4%. It indicates that the proposed NTSM controller not only maintains a smaller tracking error but also ensures faster error convergence, which in turn leads to quicker system stabilization.

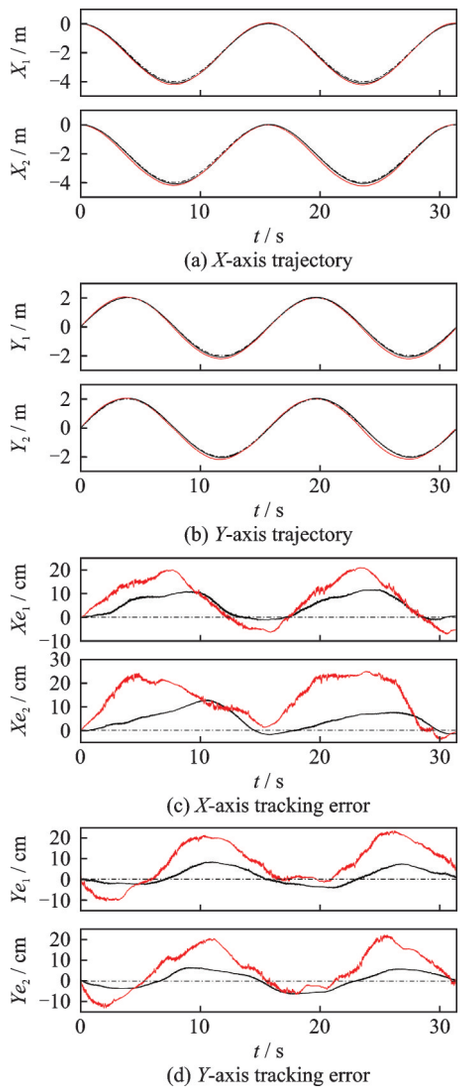

Fig.4 Control performance comparisons of our NTSM (black solid) and PID (red solid) under Experiment 1

Table 3 Comparison of controller performance cm

Controller	Index	Xe_1	Xe_2	Ye_1	Ye_2
NTSM	IAE	175	163	115	120
	ITAE	2 731	2 478	1 993	1 968
	ISE	1472	1210	574	543
PID	IAE	323	466	344	304
	ITAE	4 884	7 049	5 945	4 866
	ISE	4 394	8 521	5 314	3 993
NTSM with disturbance	IAE	207	180	125	121
	ITAE	3 061	2 637	2 136	1 769
	ISE	1 782	1 476	635	550
NTSM without DCC	IAE	188	175	133	137
	ITAE	2 859	2 636	2 119	2 127
	ISE	1 713	1 343	705	729

In Experiment 2, to validate the algorithm's robustness, the robotic arm performs swinging motions during flight to introduce disturbances. Fig.5

presents a comparison of the NTSM controller's trajectory tracking performance with and without this robotic arm disturbance. As indicated in Table 3, when subjected to the robotic arm's swinging motion, the observed maximum increases in IAE, ITAE and ISE are 18.3%, 12.1% and 21.0%, respectively. These findings effectively demonstrate the robustness of the proposed controller.

The results of Experiment 3 are presented in Fig.6, where Xe_{s1} and Ye_{s1} denote the synchronization errors of the first aerial manipulator along the x- and y-axes, respectively, while Xe_{s2} and Ye_{s2} denote

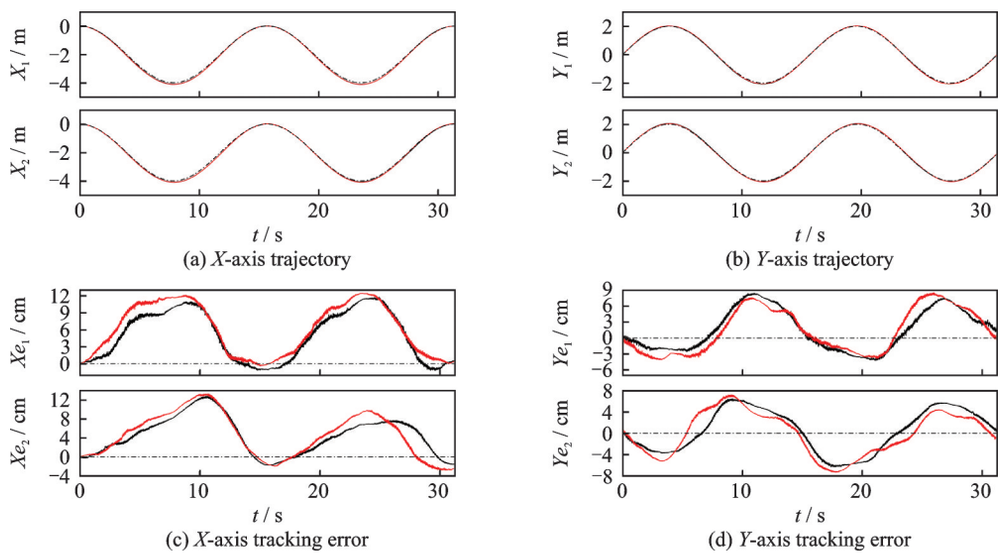

Fig.5 Comparisons of the proposed NTSM without disturbances (black solid) and with disturbances (red solid) under Experiment 2

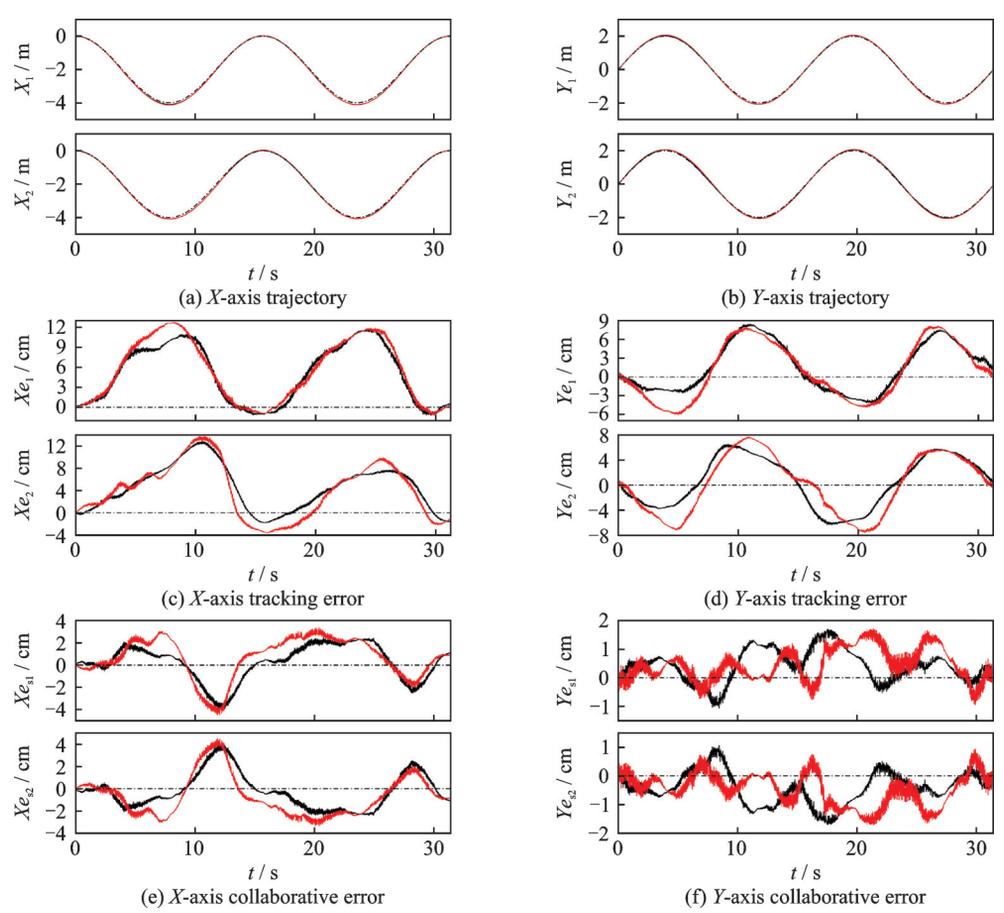

Fig.6 Control performance comparisons of the proposed NTSM with DCC (black solid) and without DCC (red solid) under Experiment 3

those of the second aerial manipulator. The IAE, ITAE and ISE of the tracking error are detailed in Table 3. As observed from Fig.6, both control configurations exhibit good tracking performance.

However, the incorporation of the DCC leads to noticeable performance improvements, particularly during direction reversals. Furthermore, Table 4 reveals that when the collaborative control component is deactivated, the IAE, ITAE and ISE of the collaborative error increase by 22.7%, 13.1%, and 41.9% along the X-axis, respectively, and by 5%, 24.1%, and 11.8% along the Y-axis, respectively. These findings demonstrate the effectiveness of the proposed collaborative control strategy. Theoretically, this improvement is attributed to the DCC scheme, which introduces a synchronization error term e_s into the control law. This term functions as a dynamic coupler, when an individual agent's error deviates from the group average, it generates a corrective control action to pull the agent back towards the collective behavior, thereby actively reducing inter-agent discrepancies and improving overall collaborative performance.

Table 4 Comparison of collaborative error cm

Controller	Index	Xe_{s1}	Xe_{s2}	Ye_{s1}	Ye_{s2}
NTSM	IAE	44	44	20	20
	ITAE	757	757	294	294
	ISE	86	86	17	17
NTSM without DCC	IAE	54	54	21	21
	ITAE	856	856	365	365
	ISE	122	122	19	19

5 Conclusions

This paper proposes a NTSM controller that integrates TDE and a DCC scheme for the collaborative control of aerial platforms in the system of multiple aerial manipulators. It does not rely on a precise dynamic model and exhibits strong practical applicability. Subsequently, the stability is analyzed using the Lyapunov method. The experimental results demonstrate that the proposed NTSM controller outperforms the TDE-enhanced PID controller, achieving higher control precision and faster error convergence speed. In the presence of disturbances from the robotic arm's swinging motion, the NTSM controller effectively maintains its performance, underscoring its strong robustness. Moreover, the DCC scheme significantly reduces collaborative errors between the aerial manipulator units and improves their overall collaborative performance.

Based on the research findings presented above, the collaborative performance among multiple aerial manipulators is effectively demonstrated. Future work will involve conducting experimental research on collaborative grasping tasks performed by multiple aerial manipulators.

References

[1] SONG Guangming, HAO Shuang, JI Zichao, et al. Research progress of aerial manipulators for contact-based operations[J]. Journal of Mechanical Engineering, 2025, 61(3): 197-211. (in Chinese)

[2] KIM S, SEO H, SHIN J, et al. Cooperative aerial manipulation using multirotors with multi-DOF robotic arms[J]. IEEE/ASME Transactions on Mechatronics, 2018, 23(2): 702-713.

[3] OLLERO A, TOGNON M, SUAREZ A, et al. Past, present, and future of aerial robotic manipulators[J]. IEEE Transactions on Robotics, 2022, 38(1): 626-645.

[4] RUGGIERO F, LIPPIELLO V, OLLERO A. Aerial manipulation: A literature review[J]. IEEE Robotics and Automation Letters, 2018, 3(3): 1957-1964.

[5] TUTSOY O, ASADI D, AHMADI K, et al. Minimum distance and minimum time optimal path planning with bioinspired machine learning algorithms for faulty unmanned air vehicles[J]. IEEE Transactions on Intelligent Transportation Systems, 2024, 25(8): 9069-9077.

[6] YAN Yonggang, LI Xinfei, SHEN Zhiyuan, et al. A high-precision risk analysis model of logistics UAV network with multiple constraining factors[J]. Transactions of Nanjing University of Aeronautics and Astronautics, 2024, 41(2): 218-232.

[7] ORSAG M, KORPELA C, BOGDAN S, et al. Dexterous aerial robots: Mobile manipulation using unmanned aerial systems[J]. IEEE Transactions on Robotics, 2017, 33(6): 1453-1466.

[8] XU M X, HU A, WANG H S. Image-based visual impedance force control for contact aerial manipulation[J]. IEEE Transactions on Automation Science and Engineering, 2023, 20(1): 518-527.

[9] WANG Y Y, CHEN J W, YAN F, et al. Adaptive super-twisting fractional-order nonsingular terminal sliding mode control of cable-driven manipulators[J]. ISA Transactions, 2019, 86: 163-180.

[10] YOUCEF-TOUMI K, ITO O. A time delay controller for systems with unknown dynamics[C]//Proceedings of 1988 American Control Conference. Atlanta, GA, USA: IEEE, 2009: 904-913.

[11] WANG Y Y, YAN F, CHEN J W, et al. A new adaptive time-delay control scheme for cable-driven manipulators[J]. IEEE Transactions on Industrial Informatics, 2019, 15(6): 3469-3481.

[12] BAEK J, KWON W, KIM B, et al. A widely adaptive time-delayed control and its application to robot manipulators[J]. IEEE Transactions on Industrial Electronics, 2019, 66(7): 5332-5342.

[13] JIN M L, LEE J, AHN K K. Continuous nonsingular terminal sliding-mode control of shape memory alloy actuators using time delay estimation[J]. IEEE/ASME Transactions on Mechatronics, 2015, 20(2): 899-909.

[14] WANG Y Y, GU L Y, XU Y H, et al. Practical tracking control of robot manipulators with continuous fractional-order nonsingular terminal sliding mode[J]. IEEE Transactions on Industrial Electronics, 2016, 63(10): 6194-6204.

[15] CHOI J, KWON W, LEE Y S, et al. Adaptive time-delay estimation error compensation for application to robot manipulators[J]. Control Engineering Practice, 2024, 151: 106029.

[16] FERNANDES R, APOLINÁRIO J, SEIXAS J M. Enhancing TDE-based drone DoA estimation with genetic algorithms and zero cyclic sum[C]//Proceedings of Anais do XVI Congresso Brasileiro de Inteligência Computacional. [S.l.]: SBIC, 2023: 1-7.

[17] ZHANG X, LIU J G, TONG Y C, et al. Attitude decoupling control of semifloating space robots using time-delay estimation and supertwisting control[J]. IEEE Transactions on Aerospace and Electronic Systems, 2021, 57(6): 4280-4295.

[18] ZHANG Z B, LI X H, WANG X, et al. TDE-based adaptive integral sliding mode control of space manipulator for space-debris active removal[J]. Aerospace, 2022, 9(2): 105.

[19] WANG Y Y, ZHU K W, CHEN B, et al. Model-free continuous nonsingular fast terminal sliding mode control for cable-driven manipulators[J]. ISA Transactions, 2020, 98: 483-495.

[20] VAN M, DO X P, MAVROVOUNIOTIS M. Self-tuning fuzzy PID-nonsingular fast terminal sliding mode control for robust fault tolerant control of robot manipulators[J]. ISA Transactions, 2020, 96: 60-68.

[21] LEE J, CHANG P H, JIN M L. Adaptive integral sliding mode control with time-delay estimation for robot manipulators[J]. IEEE Transactions on Industrial Electronics, 2017, 64(8): 6796-6804.

[22] WANG Y Y, LI B B, YAN F, et al. Practical adaptive fractional-order nonsingular terminal sliding mode control for a cable-driven manipulator[J]. International Journal of Robust and Nonlinear Control, 2019, 29(5): 1396-1417.

[23] WANG Y Y, LIU L F, WANG D, et al. Time-delay control using a novel nonlinear adaptive law for accurate trajectory tracking of cable-driven robots[J]. IEEE Transactions on Industrial Informatics, 2020, 16(8): 5234-5243.

[24] BAEK S, BAEK J, HAN S. An adaptive sliding mode control with effective switching gain tuning near the sliding surface[J]. IEEE Access, 2019, 7: 15563-15572.

[25] WANG Y Y, JIANG S R, YAN F, et al. Sliding mode control of a newly designed cable-driven manipulator with time delay estimation[C]//Proceedings of 2017 17th International Conference on Control, Automation and Systems (ICCAS). Jeju, Korea: IEEE, 2017: 1605-1609.

[26] CHAWENGKRITTAYANONT P, PUKDEBOON C, KUNTANAPREEDA S, et al. Smooth second-order sliding mode controller for multivariable mechanical systems[J]. SN Applied Sciences, 2021, 3(10): 816.

[27] XIONG J J, ZHANG G B. Global fast dynamic terminal sliding mode control for a quadrotor UAV[J]. ISA Transactions, 2017, 66: 233-240.

[28] YAO Q J, LI Q, HUANG M J, et al. Predefined-time trajectory tracking control of free-flying space manipulator subject to uncertainties and disturbances[J]. Robotics and Autonomous Systems, 2024, 177: 104699.

[29] ISLAM S. NTSM based finite-time consensus control for a networked of quadrotor vehicles with disturbances[C]//Proceedings of 2023 IEEE International Conference on Industrial Technology (ICIT). Orlando, FL, USA: IEEE, 2023: 1-6.

[30] BRAN C B, IOB P, CENEDESE A, et al. Non-singular terminal sliding mode control for a three-link manipulator with variable mass[C]//Proceedings of 2023 IEEE Conference on Control Technology and Applications (CCTA). Bridgetown, Barbados: IEEE, 2023: 333-338.

[31] SUN Y C, WANG Y Y, CUI B Y, et al. Fuzzy disturbance observer based NTSM attitude control for combined spacecraft[C]//Proceedings of 2022 International Conference on Autonomous Unmanned Systems (ICAUS 2022). Singapore: Springer, 2023: 1931-1940.

[32] SHAO K, TANG R C, XU F, et al. Adaptive sliding mode control for uncertain Euler-Lagrange systems with input saturation[J]. Journal of the Franklin Institute, 2021, 358(16): 8356-8376.

[33] MAHONY R, KUMAR V, CORKE P. Multirotor aerial vehicles: Modeling, estimation, and control of quadrotor[J]. IEEE Robotics & Automation Magazine, 2012, 19(3): 20-32.
[34] ISLAM R UL, IQBAL J, KHAN Q. Design and comparison of two control strategies for multi-DOF articulated robotic arm manipulator[J]. Journal of Control Engineering and Applied Informatics, 2014, 16(2): 28-39.
[35] AFIFA R, ALI S, PERVAIZ M, et al. Adaptive backstepping integral sliding mode control of a MIMO separately excited DC motor[J]. Robotics, 2023, 12(4): 105.

Acknowledgements This work was supported in part by the National Natural Science Foundation of China (Nos.52575120,52175097) and Key Research and Development Program of Zhejiang (No.2024SSYS0089).

Authors

The first author Mr. **WU Zhiyu** received the B.S. degree in College of Mechanical and Electrical Engineering from Nanjing University of Aeronautics and Astronautics, Jiangsu, China, in 2023. He is currently studying towards the M.S. degree in the same university. His research interests include multiple aerial manipulators, position and attitude tracking control of UAV.

The corresponding author Dr. **WANG Yaoyao** received the B.S. degree in mechanical engineering from Southeast University, Nanjing, China, in 2011, and the Ph.D. degree in mechanical engineering from Zhejiang University, Hangzhou, China, in 2016. He is currently an associate professor with College of Mechanical and Electrical Engineering, Nanjing University of Aeronautics and Astronautics, Nanjing. His current research interests include robust control and adaptive control of mechatronic systems and design and control of cable-driven systems, such as cable-driven underwater manipulators and cable-driven flying manipulators.

Author contributions Mr. **WU Zhiyu** designed the research, conducted the experiments, analyzed the data, and wrote the manuscript. Dr. **WANG Yaoyao** designed the article structure, provided funding support, and participated in the manuscript revision. Mr. **WANG Hanzhuo** participated in the experiments. Prof. **CHEN Jiawang** provided funding support and participated in manuscript revision. Mr. **SUN Lizhuang** provided funding support and participated in manuscript revision. All authors commented on the manuscript draft and approved the submission.

Competing interests The authors declare no competing interests.

(Production Editor: XU Chengting)

基于非奇异终端滑模的多飞行机械臂时延协同控制

吴志雨[1]，王尧尧[1,2]，王汉卓[1]，陈家旺[3]，孙立壮[4]

(1.南京航空航天大学机电学院,南京 210016,中国; 2.机械结构力学及控制国家重点实验室, 南京 210016, 中国; 3.东海实验室,舟山 316021,中国; 4.中国机械总院集团北京机电研究所有限公司,北京 100044,中国)

摘要:为提高多飞行机械臂系统在复杂综合扰动下的轨迹跟踪精度、同步协调能力和鲁棒控制性能,针对系统非线性强、耦合关系复杂及外部扰动不确定等问题,本文提出了一种基于时延估计(Time-delay estimation, TDE)、偏差耦合控制(Deviation coupling control, DCC)和非奇异终端滑模(Nonsingular terminal sliding, NTSM)的控制方法。该方法利用时延估计对系统未知动态和综合扰动进行在线补偿,引入偏差耦合控制增强多飞行机械臂之间的协调同步能力,并结合非奇异终端滑模控制提高系统的收敛速度和鲁棒性。同时,基于李雅普诺夫稳定性理论对所设计控制器的稳定性进行了证明。随后,基于多飞行机械臂系统开展对比实验,并以绝对误差积分(Integral of absolute error, IAE)、时间加权绝对误差积分(Integral of time-weighted absolute error, ITAE)和平方误差积分(Integral of squared error, ISE)作为性能评价指标。实验结果表明,与基于TDE的PID控制器相比,所提控制器在IAE、ITAE和ISE指标上分别至少降低了45.8%、44.1%和66.5%,能够有效提升多飞行机械臂系统在复杂扰动条件下的跟踪精度、同步性能和整体控制效果。

关键词:多飞行机械臂;时延估计;终端滑模;协同控制

研究亮点:

1.构建了一种面向多飞行机械臂协同控制的TDE-DCC-NTSM复合控制框架,提高了系统在复杂扰动下的协同作业能力。

2.在轨迹跟踪性能方面,所提控制器相较于TDE-PID控制器在IAE、ITAE和ISE方面分别至少降低45.8%、44.1%和66.5%;在同步协调性能方面,引入偏差耦合误差后,多飞行机械臂之间的同步误差得到进一步抑制,验证了DCC机制对协同控制性能的改善作用。